MICROBIOME OF GRAND CANYON CAVERNS, A DRY SULFURIC KARST CAVE IN ARIZONA, SUPPORTS DIVERSE EXTREMOPHILIC BACTERIAL AND ARCHAEAL COMMUNITIES

Raymond Keeler[1,2] and Bradley Lusk[2,3,*]

[1]National Speleological Society, Huntsville, AL, United States of America.
[2]Central Arizona Grotto, Phoenix, AZ, United States of America.
[3]ScienceTheEarth, Mesa, AZ, United States of America.
* Corresponding author, ScienceTheEarth@gmail.com, ORCID: 0000-0002-3094-805X.

Supplemental Material

Sample ID	Sequence	Kingdom	Phylum	Class	Order	Family	Genus	Species
GCC1	50142	3	35	73	167	276	485	630
GCC2	126481	3	44	107	261	469	891	1252
GCC3	95592	3	29	50	116	181	303	418
GCC4	70373	3	24	44	99	152	232	313
GCC5	54351	3	23	40	93	140	211	252
GCC6	44596	3	28	49	109	179	301	397
GCC7	142016	3	25	45	101	163	278	362
GCC8	103357	3	35	60	132	218	399	538
GCC9	141660	3	41	93	212	363	633	814
GCC10	126235	3	27	41	83	122	165	187
GCC11	89359	3	24	40	88	135	208	275
GCC12	44297	3	21	32	62	93	127	158
GCC13	108956	3	32	69	165	271	442	575
GCC14	133335	3	34	70	160	267	488	643

Table S1: Overview of sequencing results from all samples. The “Sequence” column reports the number of sequences observed at each site. The remaining columns show the amount of unique OTUs observed for each taxonomy level at each sampling site.

Table S2: Provides counts for classified OTUs at kingdom, phylum, class, order, family, genus, and species levels. Table is provided as a separate downloadable Excel file.

Sulfuric acid speleogenesis occurs via the reduction of elemental sulfur to create hydrogen sulfide, which is then oxidized to form sulfuric acid that catalyzes the dissolution of limestone, leading to the formation of caves and caverns (Macalady et al. 2006; Laumanns et al. 2008; Ayangbenro et al. 2018). An overview of this process is provided in Equation S1-3.

Equation S1: Microbial reduction of elemental sulfur to create hydrogen sulfide

$$2S + CH_2O + H_2O \rightarrow 2H_2S + CO_2 \quad \text{(S1)}$$

Equation S2: Hydrogen sulfide oxidizes to form sulfuric acid

$$H_2S + 2O_2 \leftrightarrow H_2SO_4 \quad \text{(S2)}$$

Equation S3: Sulfuric acid that catalyzes the dissolution of limestone

$$CaCO_3 \text{ (limestone)} + H_2SO_4 \rightarrow CaSO_4 + CO_2 + H_2O \quad \text{(S3)}$$

Dissimilatory metal reducing and/or oxidizing bacteria are able to use Fe or Mn as an electron source or as a terminal electron acceptor, as shown in Equations S4-S7.

Equation S4: Microbial oxidation of ferrous hydroxide to ferric iron (hematite) (Snoeyink and Jenkins 1980).

$$4Fe(OH)_2 + O_2 \rightarrow 4H_2O + 2Fe_2O_3 \quad \text{(S4)}$$

Equation S5: Microbial reduction of ferric iron (hematite) to ferrous iron (magnetite) (Weber et al. 2006; Gao et al 2019).

$$3Fe_2O_3 + H_2 \rightarrow 2Fe_3O_4 + H_2O \quad \text{(S5)}$$

Equation S6: Microbial reduction of manganese (IV) oxides to manganese (II) oxides (Myers and Nealson 1988; Zhang et al. 2002; Wang et al. 2009).

$$Mn(IV) + H_2 \rightarrow Mn(II) + 2H+ \quad \text{(S6)}$$

Equation S7: Microbial oxidation of manganese (II) oxides to manganese (IV) oxides (Erlich 1980; Caspi et al. 1998).

$$Mn(II) + \tfrac{1}{2}O_2 + H_2O \rightarrow MnO_2 + 2H+ \quad \text{(S7)}$$

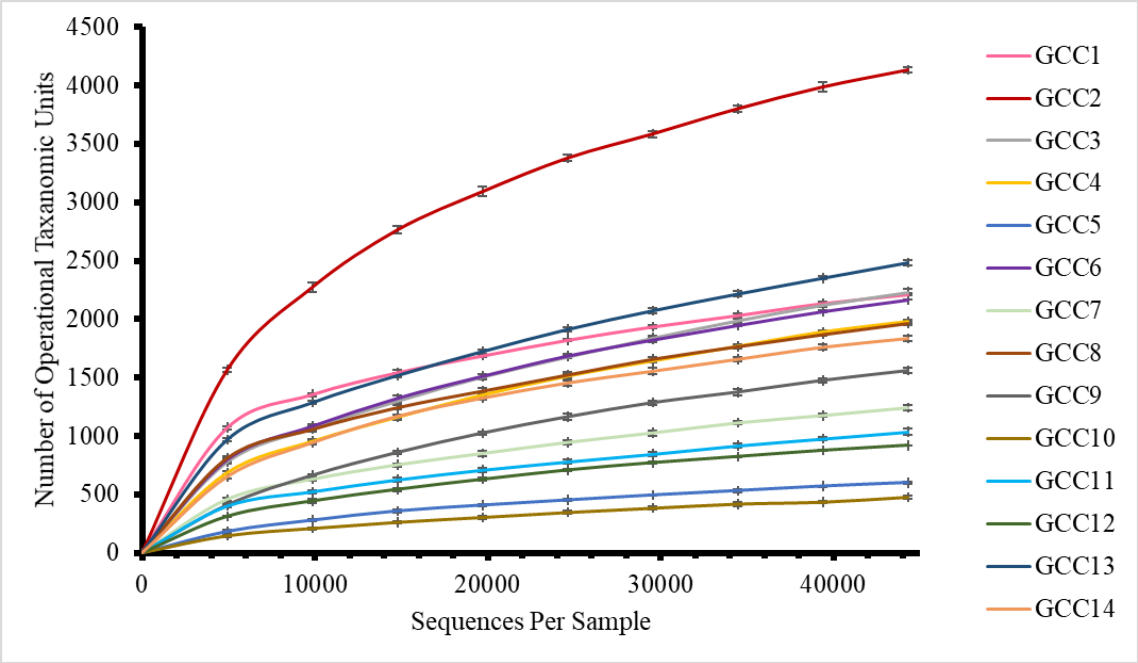

Figure S1: Rarefaction curve for α-diversity in 14 samples collected in Grand Canyon Caverns. Number of OTUs determined using a 97% cutoff. Standard deviation is indicated by black bars. (For an overview of each sample, see Table S1.)

Speleosol samples collected at 14 sites in the cave varied in color and consistency (Fig. 3). Raman spectroscopy was used to determine the mineral contents of each sample (Table 1) by comparing spectra to the RRUFF™ Project database using the CrystalSleuth Application Version: May 19, 2008 (Laetsch and Downs, 2006). Samples were divided into three consistency categories including powder (individual particle diameters < 1 mm), pebbles (individual particle diameters > 1 mm < 5 mm), and crystals (individual particle diameters > 5 mm). Sample GCC 1 is a grey powder consisting primarily of calcite (97% match at 514nm and 92% match at 785nm), GCC 2 is a mixture of tan powder and crystals consisting primarily of calcite (99% match at 514nm and 94% match at 785nm) and paraspurrite (93% match at 785nm), GCC 3 is orange pebbles consisting primarily of calcite (98% match at 514nm), GCC 4 is a mixture of brown and grey pebbles consisting primarily of calcite (97% match at 514nm), GCC 5 is orange pebbles consisting primarily of calcite (99% match at 514nm and 96% match at 785nm), GCC 6 is deep red crystals consisting primarily of quartz (99% match at 514nm) and trattnerite (91% match at 785nm), GCC 7 is a deep red powder consisting primarily of quartz (99% match at 514nm), GCC 8 is a mixture of green and yellow crystals consisting primarily of calcite (97% match at 514nm), GCC 9 is pink crystals and could not be matched to the database at or above 90% for either wavelength although its closest match was gypsum (85% match at 514nm), GCC 10 is a mixture of yellow pebbles and crystals consisting primarily of calcite (96% match at 514nm), GCC 11 is a mixture of tan powder with pink crystals consisting primarily of calcite (96% match at 514nm), GCC 12 is white crystals consisting primarily of calcite (98% match at 514nm and 785nm), GCC 13 is tan pebbles consisting primarily of calcite (91% match at 514nm) and paraspurrite (92% match at 785nm), and GCC 14 is brown pebbles consisting primarily of hematite (92% match at 514nm). Filtered spectra with light images for each sample can be found in Fig. S2 GCC1-14.

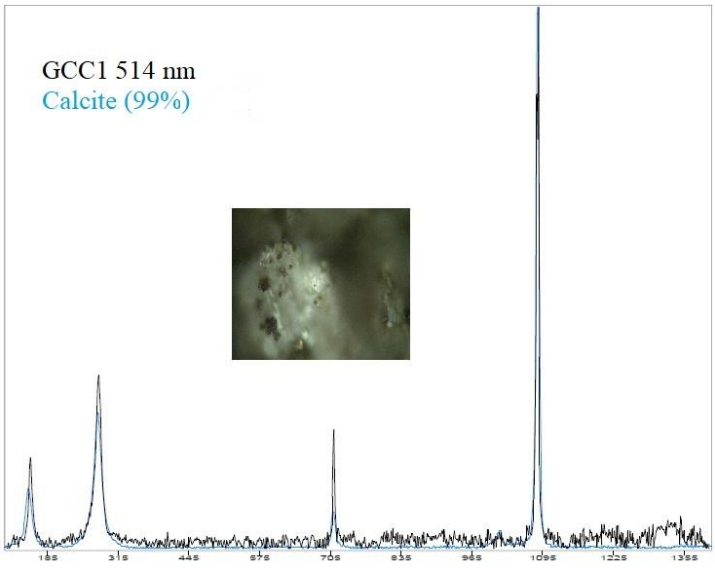
GCC1 514 nm
Calcite (99%)

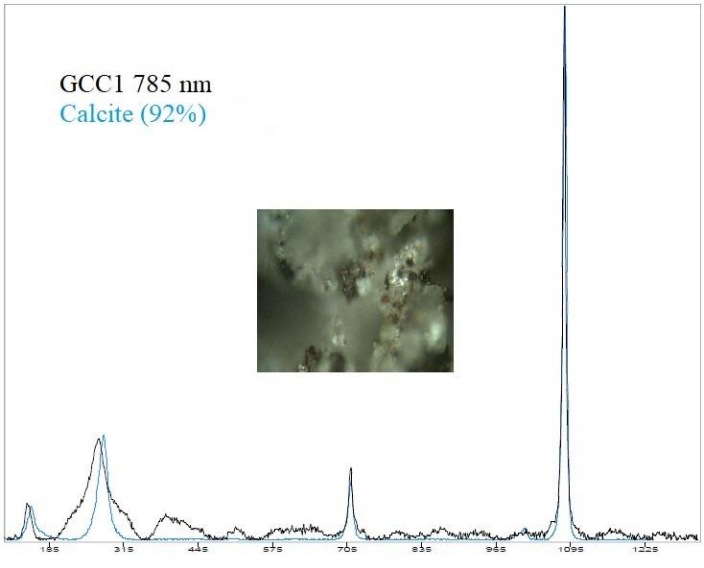
GCC1 785 nm
Calcite (92%)

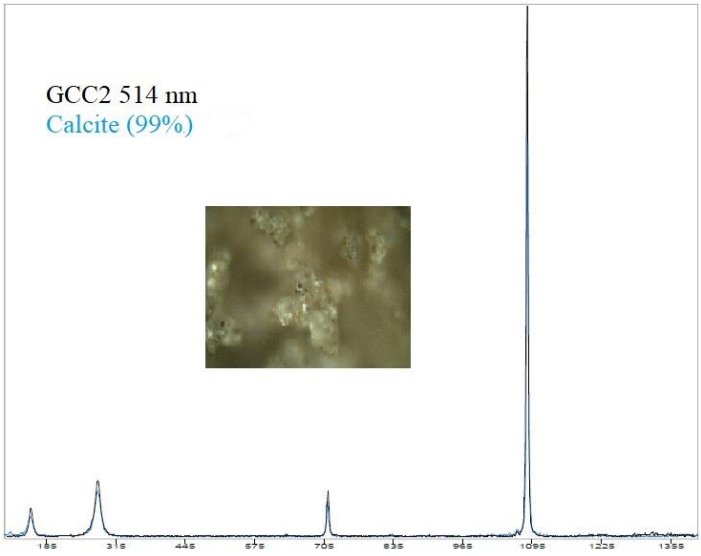
GCC2 514 nm
Calcite (99%)

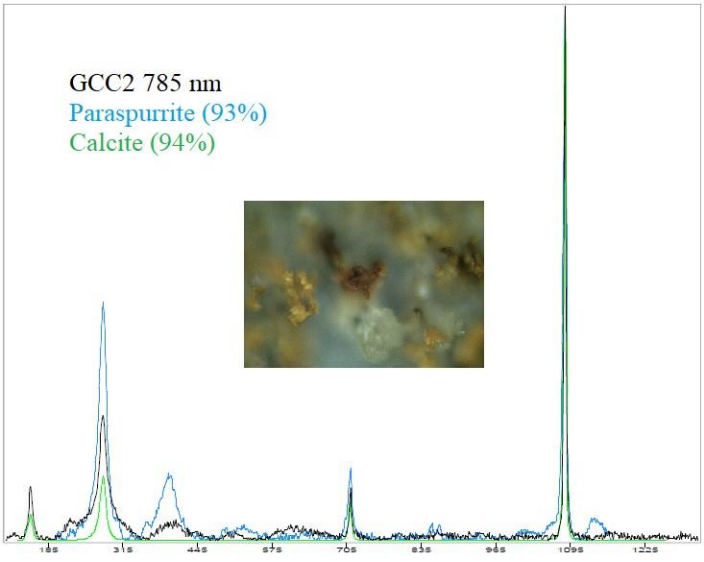
GCC2 785 nm
Paraspurrite (93%)
Calcite (94%)

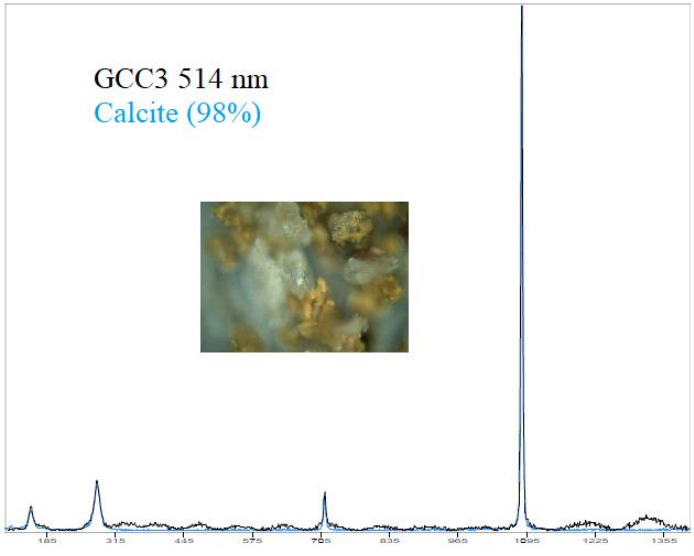
GCC3 514 nm
Calcite (98%)

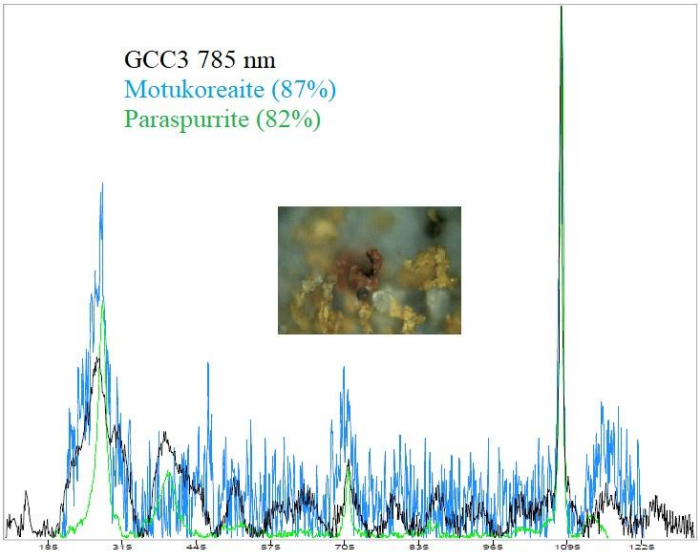
GCC3 785 nm
Motukoreaite (87%)
Paraspurrite (82%)

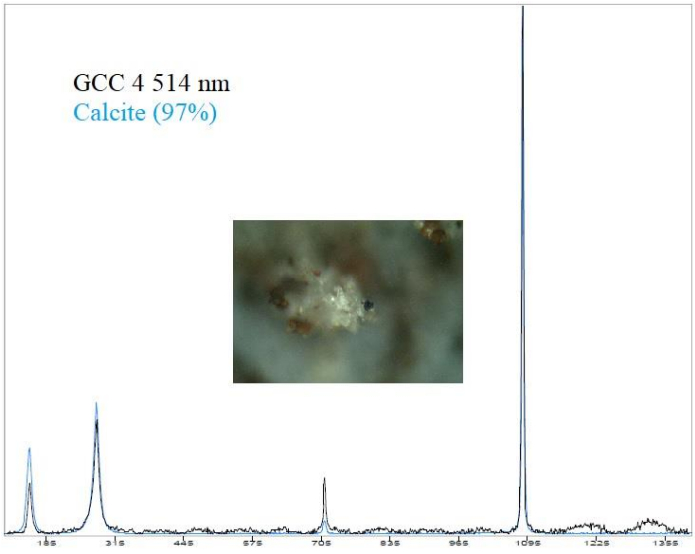
GCC 4 514 nm
Calcite (97%)

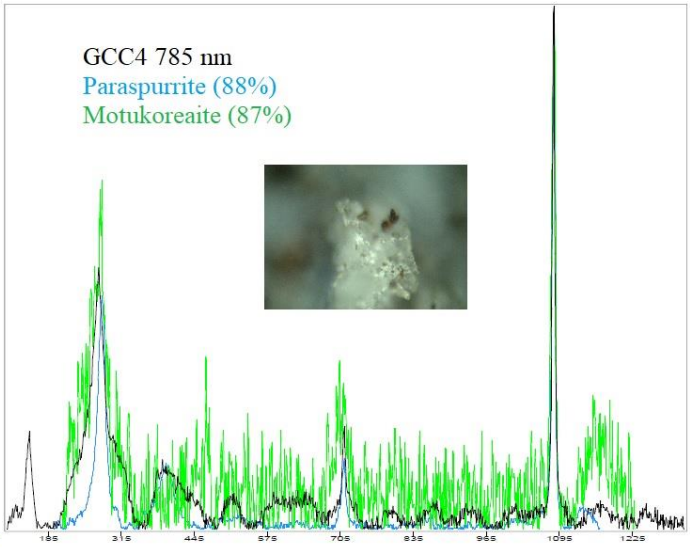
GCC4 785 nm
Paraspurrite (88%)
Motukoreaite (87%)

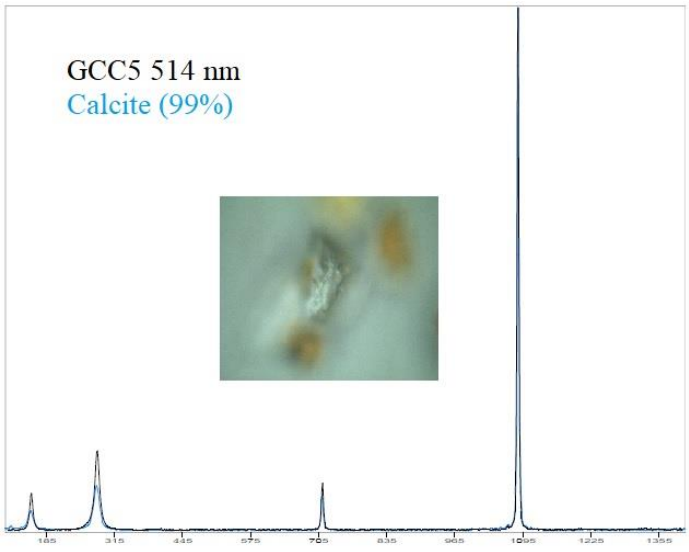
GCC5 514 nm
Calcite (99%)

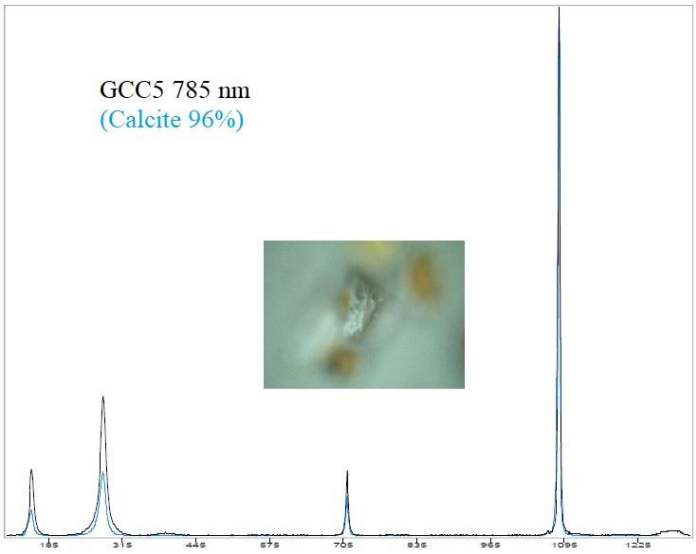
GCC5 785 nm
(Calcite 96%)

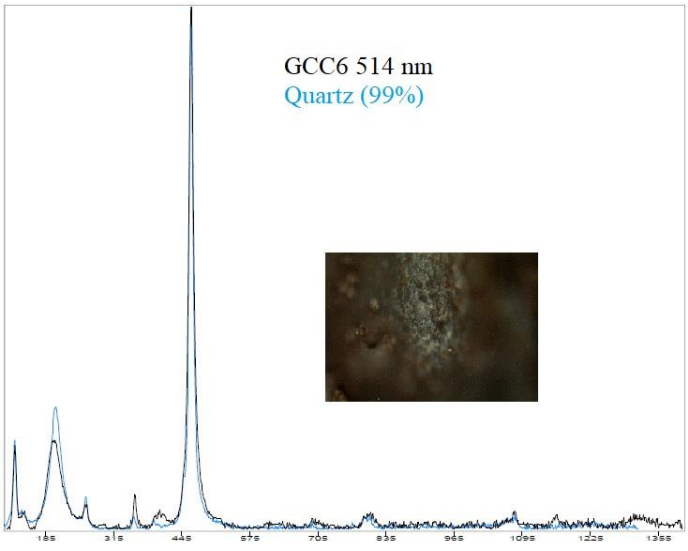
GCC6 514 nm
Quartz (99%)

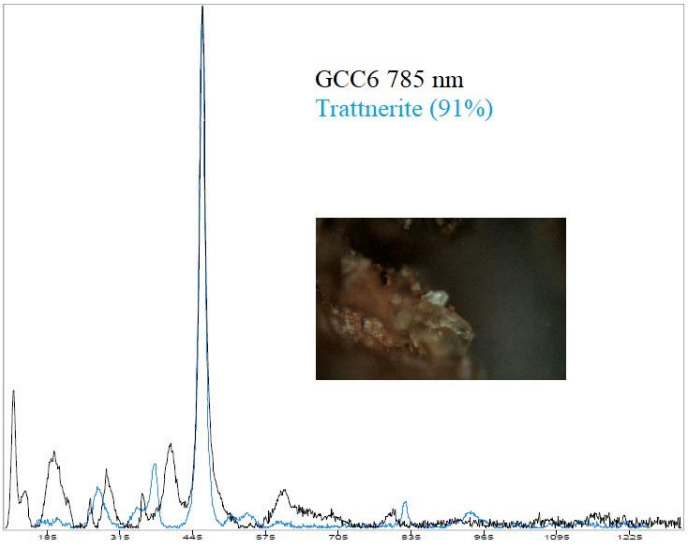
GCC6 785 nm
Trattnerite (91%)

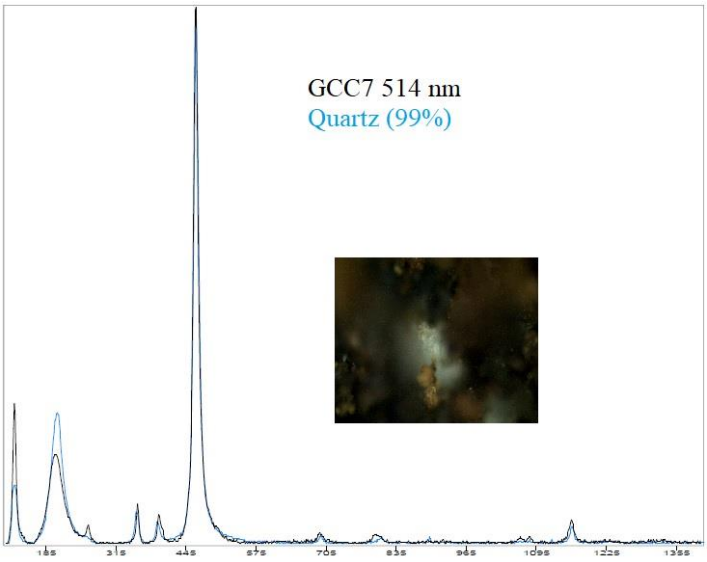
GCC7 514 nm
Quartz (99%)

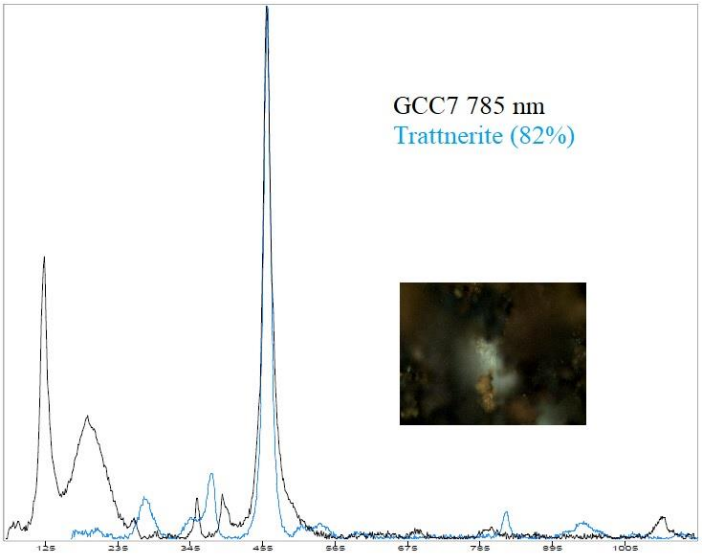
GCC7 785 nm
Trattnerite (82%)

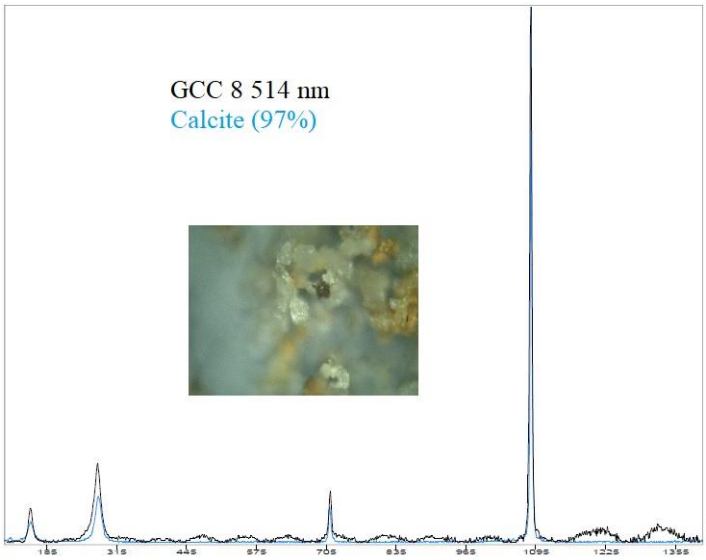
GCC 8 514 nm
Calcite (97%)

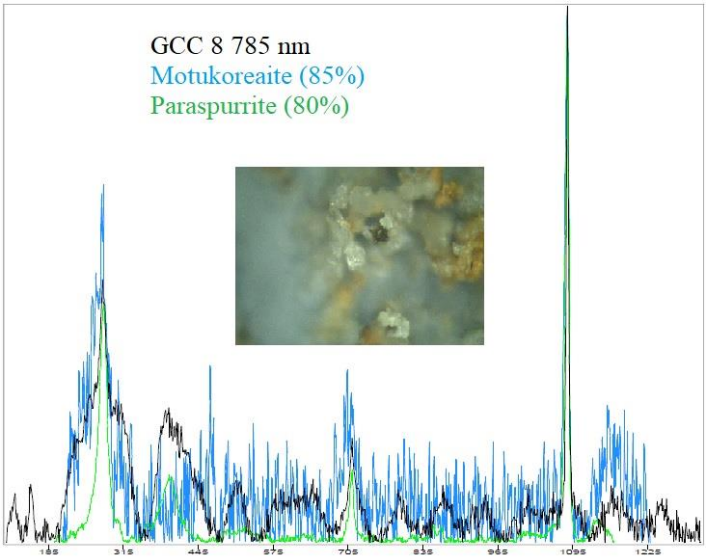
GCC 8 785 nm
Motukoreaite (85%)
Paraspurrite (80%)

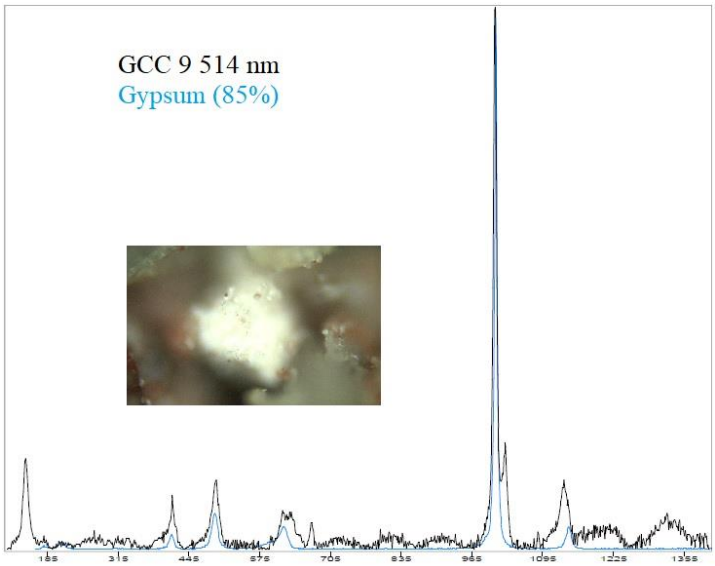
GCC 9 514 nm
Gypsum (85%)

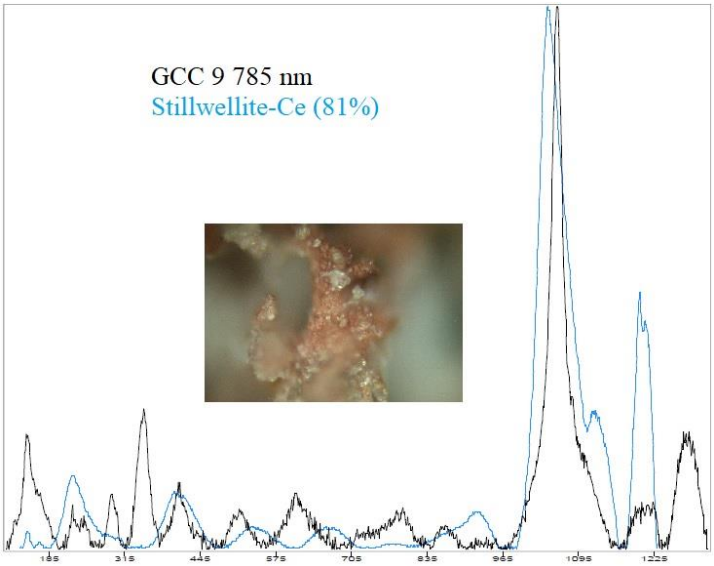
GCC 9 785 nm
Stillwellite-Ce (81%)

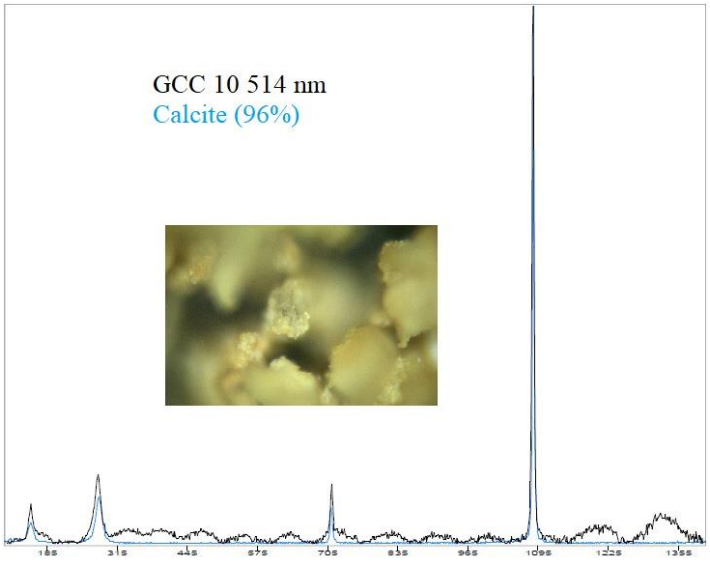
GCC 10 514 nm
Calcite (96%)

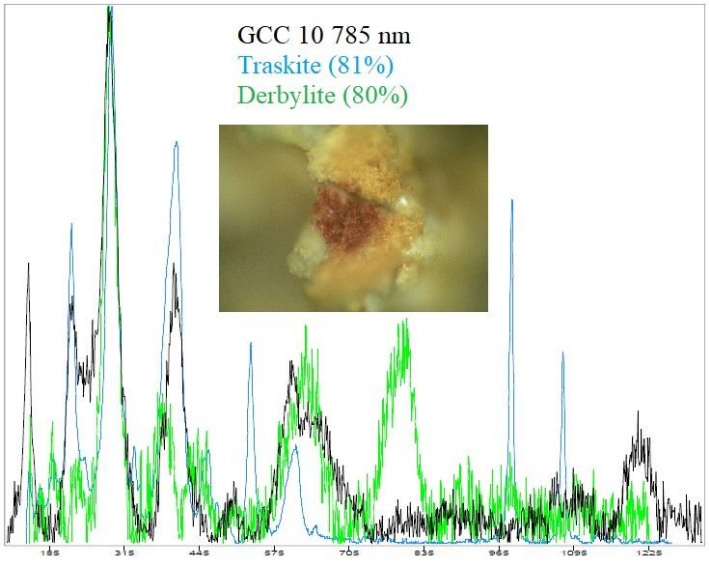
GCC 10 785 nm
Traskite (81%)
Derbylite (80%)

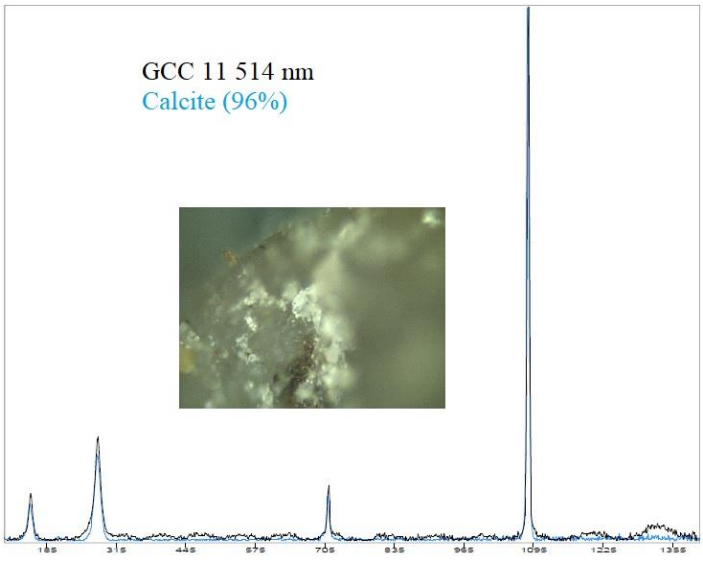
GCC 11 514 nm
Calcite (96%)

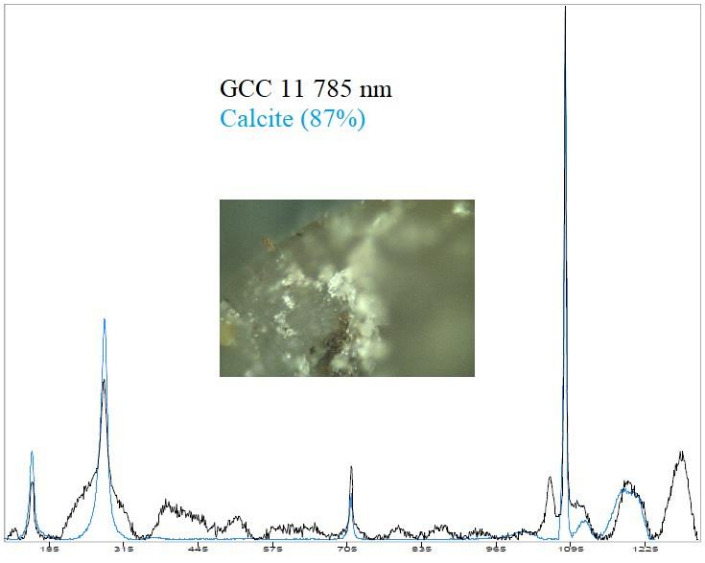
GCC 11 785 nm
Calcite (87%)

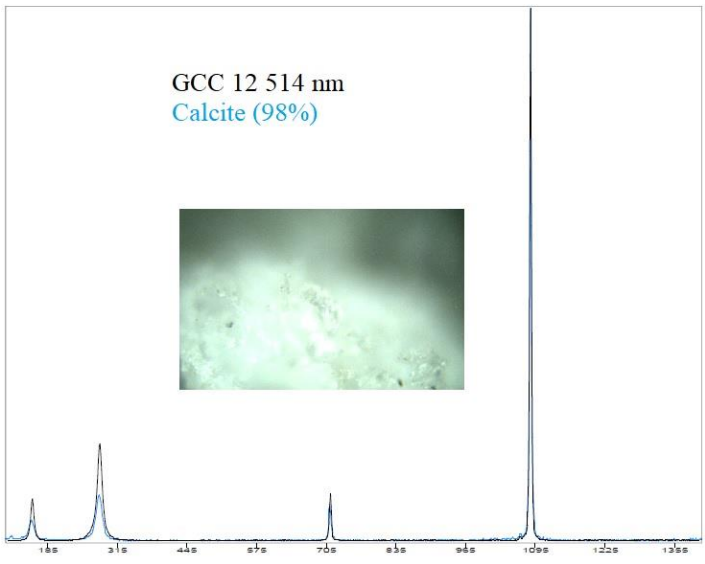
GCC 12 514 nm
Calcite (98%)

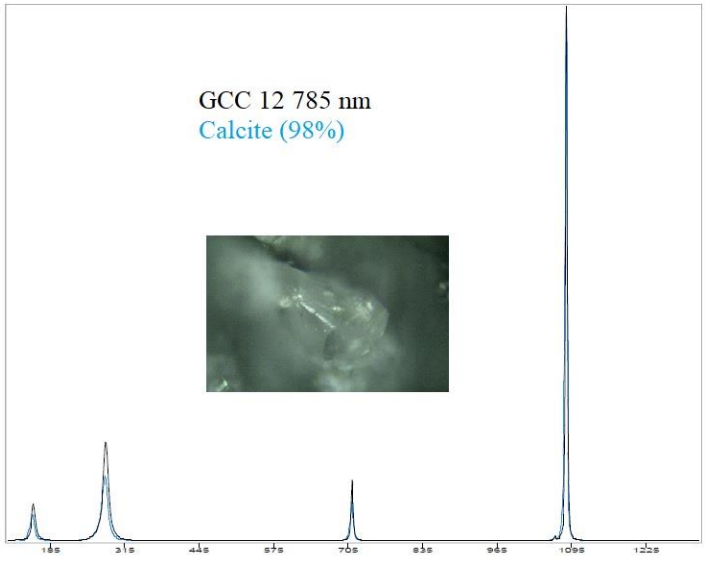
GCC 12 785 nm
Calcite (98%)

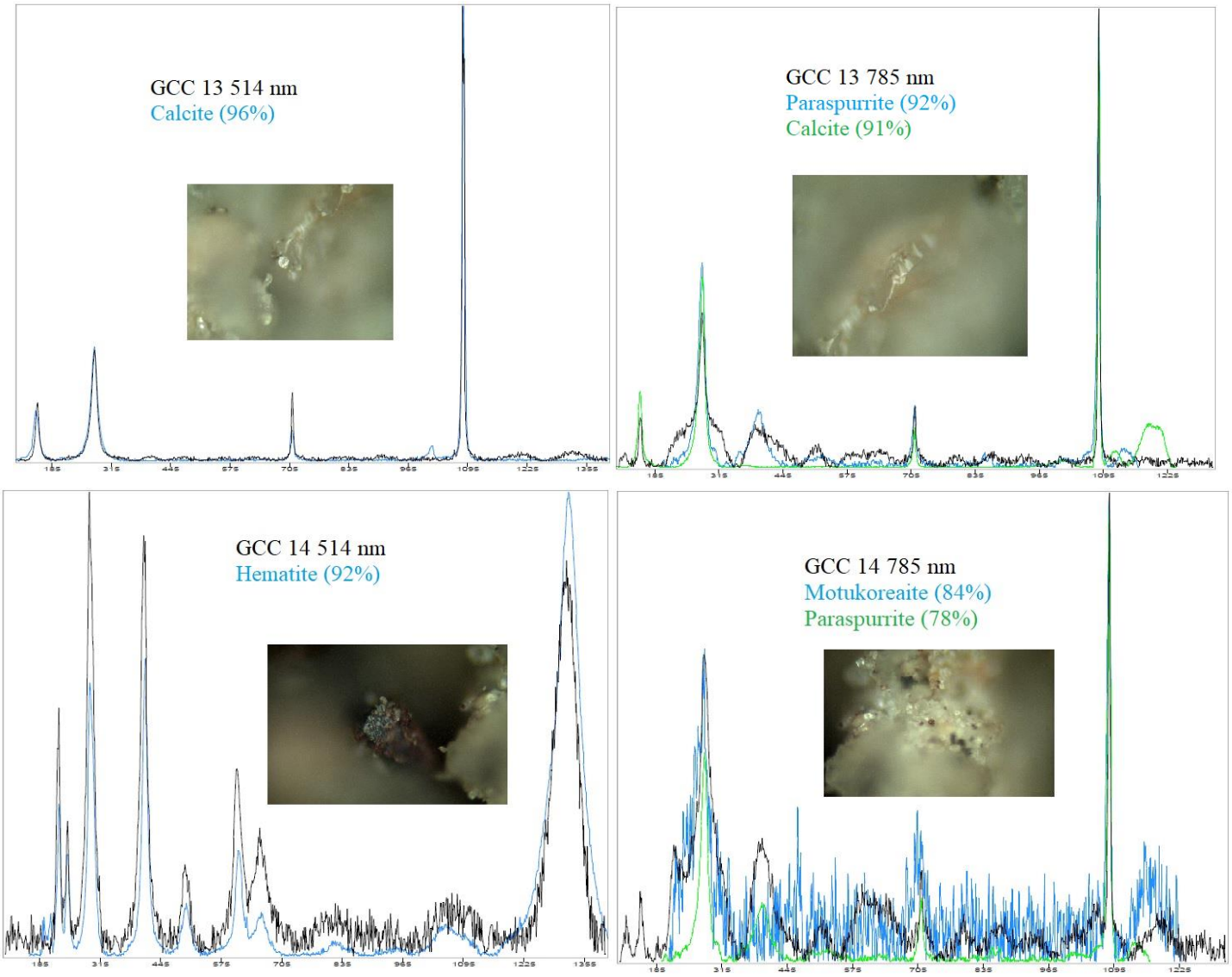

Figure S2 GCC1-14: Raman spectra at 514 nm and 785 nm for closest match compared to the RRUFF™ Project database using CrystalSleuth Application Version: May 19, 2008 after removing cosmic ray events and background subtraction. All spectra show wavenumbers from 100 to 1400 cm^{-1} on the x-axis. The y-axis represents arbitrary intensity units. Percentage match to the RRUFF™ Project database is indicated after the name of the mineral identified. RRUFF IDs for matches greater than or equal to 90% are indicated in Table 1 of the main text. In the main text, matches less than 90% are not considered a match. For all images, the black line is the experimental spectrum and the light blue and green lines (if applicable) are the RRUFF™ Project database spectra. Spectra for 514 nm and 785 nm were acquired at three separate locations per GCC sample. Spectra shown represent the highest percentage match at 514 nm and 785 nm for each sample. Inlayed light microscopy images show the location within each sample from which the spectrum was acquired. Within each sample, the 514 nm and 785 nm spectra displayed may be from the same acquisition location if this location gave the highest match for both. Otherwise, the displayed spectrum may represent a different location within the same sample, resulting in light microscopy images showing different acquisition locations.

REFERENCES:

Ayangbenro, A.S., Olanrewaju, O.S., and Babalola, O.O.. 2018, Sulfate-reducing bacteria as an effective tool for sustainable acid mine bioremediation: Frontiers in Microbiology, v. 9, no.1986, p. 1-10, doi:10.3389/fmicb.2018.01986.

Caspi, R., Tebo, B.M., and Haygood, M.G, 1998, C-Type cytochromes and manganese oxidation in *Pseudomonas putida* MnB1: Applied and Environmental Microbiology, v. 64, no. 10, p. 3549-3555.

Erlich, H.L., 1980, Different forms of microbial manganese oxidation and reduction and their environmental significance. In: Trudinger, P.A., Walter, M.R., Ralph, B.J. (eds) Biogeochemistry of ancient and modern environments. Springer, Berlin, Heidelberg, p. 327-332.

Gao, L., Lu, X., Liu, H., Li, J., Li, W., Song, R., Wang, R., Zhang, D., and Zhu, J., 2019, Mediation of extracellular polymeric substances in microbial reduction of hematite by *Shewanella oneidensis* MR-1: Frontiers in Microbiology, v. 10, no. 575, p. 1-12, doi:10.3389/fmicb.2019.00575.

Laumanns, M., Rasch, A. and Audra, P., 2008, Karst and Caves of Iraq (including the results of a 2007 Kurdish-German speleological project and an overview on hypogenic sulphidic speleogenesis): Berliner Höhlenkundliche Berichte (Berlin, Germany), v. 26, p. 1-75.

Macalady, J.L., Lyon, E.H., Koffman, B., Albertson, L.K., Meyer, K., Galdenzi, S., and Mariani, S., 2006, Dominant microbial populations in limestone-corroding stream biofilms, Frasassi Cave System, Italy: Applied and Environmental Microbiology, v. 72, no. 8, p. 5596-5609, doi:10.1128/AEM.00715-06.

Myers, C., and Nealson, K., 1988, Bacterial manganese reduction and growth with manganese oxide as the sole electron acceptor: Science, v. 240, no. 4857, p. 1319-1321, doi:10.1126/science.240.4857.1319.

Snoeyink, V.L., and Jenkins, D., 1980, Water chemistry. John Wiley & Sons, p. 380-381, ISBN 0-471-05196-9.

Wang, X., Schröder, H.C., Wiens, M., Schloßmacher, U., and Müller, W.E.G., 2009, Manganese/polymetallic nodules: micro-structural characterization of exolithobiontic- and endolithobiontic microbial biofilms by scanning electron microscopy: Micron, v. 40, no. 3, p. 350-358, doi:10.1016/j.micron.2008.10.005.

Weber, K.A., Achenbach, L.A., and Coates, J.D., 2006, Microorganisms pumping iron: anaerobic microbial iron oxidation and reduction: Nature Reviews Microbiology, v. 4, no. 10, p. 752-764, doi:10.1038/nrmicro1490.

Zhang, F., Lin, C., Bian, L., Glasby, G.P., and Zhamoida, V.A., 2002, Possible evidence for the biogenic formation of spheroidal ferromanganese concretions from the eastern Gulf of Finland, the Baltic Sea: Baltica, v. 15, p. 23-29.